Heliyon 5 (2019) e01654

Contents lists available at ScienceDirect

Heliyon

journal homepage: www.heliyon.com

Heliyon

Dielectric, conductivity and ferroelectric properties of lead-free electronic ceramic:0.6Bi($Fe_{0.98}Ga_{0.02}$)O_3-0.4$BaTiO_3$

Sugato Hajra [a,*], Manisha Sahu [a], Varsa Purohit [b], R.N.P. Choudhary [b]

[a] Department of Electronics and Instrumentation, Siksha O Anusandhan University, Bhubaneswar, 751030, India
[b] Multifunctional and Advance Materials Laboratory, Siksha O Anusandhan University, Bhubaneswar-751030, India

ARTICLE INFO

Keywords:
Materials science
Condensed matter physics

ABSTRACT

This paper presents the fabrication of a polycrystalline sample of the above electronic system by a mixed-oxide technique. The X-ray diffraction pattern show the evolution of perovskite phase (including some impurity phase). The rhombohedral symmetry and crystallite size of 42 nm were also found from the XRD. The distribution of grains in the microstructure suggests the formation of high density ceramics. The role of grains, grain boundaries and interface on resistive (impedance, electrical modulus and electrical transport) and insulating (dielectric) has been investigated over a wide range of frequencies (10^3–10^6 Hz) and temperatures (25–400 °C) using spectroscopy (dielectric, modulus and impedance) techniques. The Nyquist plot illustrates the presence of effects such as grain and grain boundary over selected temperatures. Analysis of conductivity spectra reveals that the electrical transport process of the material is influenced by charge transfer by hopping. The complex modulus spectrum also describes the dielectric relaxation of the material. The study of field dependent polarization reveals the existence of ferroelectricity in the material.

1. Introduction

In the present era, several researchers are carried out on the lead-free electroceramics with the target of achieving suitable alternative materials for lead based ceramics like lead zirconate titanate (PZT) [1]. $BiFeO_3$ (BFO), a multiferroic has been explored for its multifunctional properties which contribute towards potential use in future electronics. The European as well as several world legislations has formulated strict laws for eliminating the toxicity of lead oxide (PbO). In all sectors lead contaminates the environment as well as risk health [2]. Thus, lead free ceramics have been proposed to replace PZT by perovskite-structured (PS) materials like $BaTiO_3$ (BTO), $Bi_{1/2}Na_{1/2}TiO_3$ (BNT), $K_{1/2}Na_{1/2}NbO_3$ (KNN) or their solid solutions with various perovskites. KNN-based compounds are potential candidates to replace the PZT for device manufacturing. However, in 2016, some reports [3] reveal that the life cycle of KNN leads to consumption of energy and destruction of the environment (i.e. mining of Nb_2O_5). Thus the common term "lead-free" must be supplemented by "niobium-reduced" in spite of its non-toxic nature. Looking into this current problem more attention towards an alternative may shift towards bismuth based solid solutions including BNT, $Bi_{1/2}K_{1/2}TiO_3$, $BiZn_{1/2}Ti_{1/2}O_3$, $BiMg_{1/2}Ti_{1/2}O_3$ and BFO [4, 5, 6]. The BFO is an ecologically stable multiferroics at room temperature (RT) and has wide usage in future devices. It has generally a rhombohedral symmetry having R3c space group. It undergoes a phase transition (anti-ferromagnetic-paramagnetic) at T_{neel} = 650 K and transforms from the ferroelectric-paraelectric at a Curie temperature (T_c) = 1100 K [7]. For a BFO single crystal, there is a presence of large spontaneous polarization of 100 μC/cm^2 along the $[110]_{pc}$ direction [8]. The polycrystalline BFO, processed by mechano-chemical route, shows remnant polarization of around 20 μC/cm^2 [9]. The pure BFO suffers many drawbacks like high leakage current, thermodynamic instability, processing issues (formation of secondary/impurity phases), low piezoelectric coefficient, and difficulty in poling [10].

Nevertheless, huge attempts in overcoming the drawbacks are carried out to reveal the multifunctional properties of BFO by partial substitution of dopants at various sites (A- or B-site) of BFO. In addition, the formation of BFO-ABO_3 based solid solutions (binary, ternary, quaternary systems) also contributes towards revealing the functional properties of BFO [11]. Among many BFO-BTO solid solutions are quite promising to be utilized in high temperature device applications surpassing the ferroelectric having low T_c. There are rare reports [12] regarding the formation of a saturated ferroelectric loop in the BFO-BTO bulk ceramics as a result of the high leakage current or intrinsic ferroelectric nature of BFO.

Some past report suggests in Gallium doped BFO there is an existence

* Corresponding author.
E-mail address: sugatofl@outlook.com (S. Hajra).

https://doi.org/10.1016/j.heliyon.2019.e01654
Received 14 December 2018; Received in revised form 20 February 2019; Accepted 1 May 2019

of polar phases with Cm symmetry and super-tetragonality. However, no consistent or clear possibility of improved electrical and ferroelectric properties was addressed [13]. A report [14] on gallium doping on BTO shows the structural and dielectric properties of the synthesized sample. It suggests that the quality factor depends on the processing routes.

Based on literature, it is found that the impedance spectroscopy technique has not been adopted to give an insight into the electrical properties of BFG-BT ceramics. In this context, we have reported the resistive, conducting, ferroelectric, insulating/dielectric, morphological, molecular (Raman) and structural analysis of BFG-BT solid solution. The impedance and modulus data have been further analyzed to understand the nature of relaxation and the conduction mechanism in this system.

2. Experimental

The Ga-substituted BFO-BTO ceramics were synthesized using a mixed oxide route. The analytical grade high-purity precursor powders, such as Bi_2O_3 (99%, Loba Chemie), Fe_2O_3 (98%, Loba Chemie), $BaCO_3$ (99.99%, Central Drug House), TiO_2 (99.99%, Central Drug House), Ga_2O_3 (99.999%, Otto-Chemika-Biochemika-Reagents) have been used. The sintering at higher temperature leads to the loss of volatile oxide is compensated using an extra 2 mole % of BFO. The precursor powders were measured as per stoichiometric ratios, followed by grounding in the agate mortar and pestle. The mixing of powders basically was carried out in two stages; firstly it was mixed in dry condition, then for more homogeneity in methanol (wet) medium to combine 4 hours. The resulting dried powder was calcined at the 940 °C for 4 hours (rate of heating: 5 °C min^{-1}). Thereafter, the calcined powders were mixed with a binder (PVA, 5 weight %) to reduce the brittle nature. A uniaxial pressure of 25 MPa was applied to compact the powder into 12mm diameter pellets. The heating of the pellets was done at 600 °C for 1 hour to remove the effect of binder followed by sintering of pellets at the 950 °C for 4 hours.

X-ray diffractometer (Rigaku, SmartLab) was utilized to obtain the diffraction pattern of the prepared solid solution depicting the crystal structure information. The pattern was obtained at the slower scan rate of 4^o min^{-1} using Cu Kα radiation over a wide Braggs angle (2θ). The refinement of the obtained XRD spectra was carried out using commercial software (MAUD). The surface of the sintered pellet was polished and coating of gold was done to obtain the natural surface microstructure of BFG-BT. The scanning electron microscope (EVO18, Ziess) was employed for this purpose. The gold coating basically eliminates the charging effect. For measurement of the electrical parameters one of the sintered pellets were smoothed via polishing. The thickness of the sample was below 1.5 mm to achieve high electrical field during the ferroelectric measurements. High purity silver paint (Sigma Aldrich) was painted onto both pellet surfaces. The ferroelectric hysteresis loop was obtained using advanced ferroelectric system aixACT systems, Germany. The electrical parameters were basically evaluated at room temperature using an impedance meter (PSM N4L, UK) over a range of frequency (1 kHz-1 MHz) as a function of temperature (25 °C -400 °C).

3. Results and discussion

3.1. Structural and morphology

Figure 1 depicts the structural (XRD) pattern of BFG-BT at room temperature. The crystalline nature and structural data (details in Table 1) of BFG-BT can be obtained from XRD data with the help of 'POWDMULT' software. The homogeneity and crystallization of the prepared sample can be identified from the peaks of narrow and sharp intensities. The refined lattice parameters of the least-squares method was noted as, a = 3.988 Å, c = 3.983 Å, tetragonality factor (c/a) = 0.998 and volume = 63.37 $(Å)^3$. The refinement of the structure is conducted by the software package MAUD (Fig. 2). The crystallographic information file is used to obtain a pattern which is further compared/simulated with an experimental pattern. The residual value of R_w (%) = 12.035, R_{nw} (%) = 0.1203, R_b (%) = 9.1633 and sigma = 3.199 is obtained from refinement. The crystallographic information file (CIF: NIMS_MatNavi_4295346521_1_2) of rhombohedral symmetry (R3c spacegroup) of $BiFeO_3$ is used for refinement of structure. The small intensity peaks corresponding to the impurities $Bi_{25}FeO_{39}$ and $Bi_2Fe_4O_9$ are marked by * and # respectively [15]. The crystallite size (Cs) was calculated through the broadening (β) of reflection peaks (at half height), a position at the Bragg angle (2θ) and the wavelength (λ) in Scherrer equation (Equation 1) [16, 17]:

$$Cs = u\lambda/\beta\cos\theta \quad (1)$$

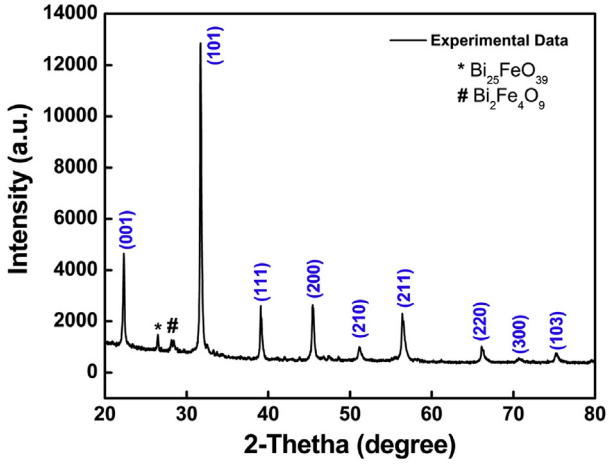

Fig. 1. XRD diffraction pattern of BFG-BT at room temperature. The small intensity peaks corresponding to the impurities $Bi_{25}FeO_{39}$ and $Bi_2Fe_4O_9$ are marked by * and # respectively.

Table-1
Comparison of observed and calculated d-values of major reflection plane with observed relative intensity (I/I_0) at room temperature of $0.6Bi(Fe_{0.98}Ga_{0.02})O_3$-$0.4BaTiO_3$.

Peak	d-spacing (obs.) (Å)	d-spacing (cal.) (Å)	I/I_o	h	k	l
1	3.9832	3.9832	36.10	0	0	1
2	2.8185	2.8185	100	1	0	1
3	2.3029	2.3018	20.20	1	1	1
4	1.9943	1.9944	20.55	2	0	0
5	1.7839	1.7838	7.78	2	1	0
6	1.6300	1.6280	17.88	2	1	1
7	1.4120	1.4102	7.89	2	2	0
8	1.3323	1.3296	4.42	3	0	0
9	1.2604	1.2548	5.90	1	0	3

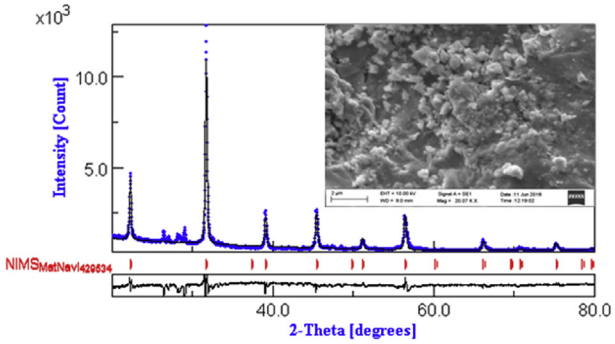

Fig. 2. Rietveld refined XRD pattern (observed (denoted by a blue dot), calculated (denoted by a black solid line) patterns and difference curve (the bottom black line)) and (inset) surface morphology and density of sintered pellet.

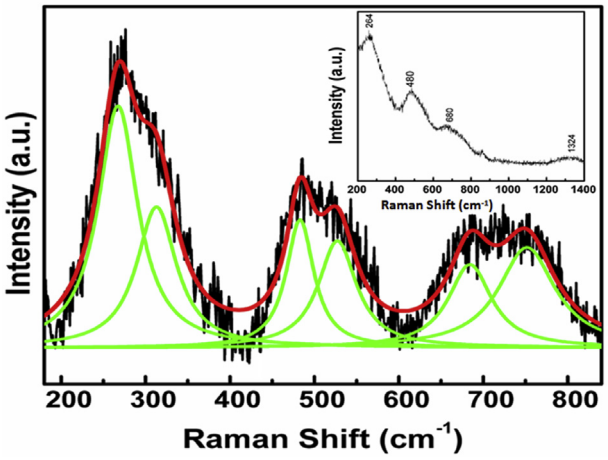

Fig. 3. Deconvoluted Raman modes within 400–800 cm^{-1} and (inset) Room temperature Raman spectra of BFG-BT.

where symbols have a similar meaning; Scherrer constant (u) = 0.89. The average crystallite size was noted as 42 nm. Fig. 2 inset suggests the surface microstructure of the natural surface of the sintered pellet. The ceramic surface has uneven (shape and size) and randomly scattered/oriented grains on the surface of the pellet. The relative density calculated is found to be 90% derived from the XRD pattern. A highly dense ceramic is obtained which influence the physical properties of the sample. No cracks were seen on the surface of the sintered pellet.

3.2. Raman analysis

X-ray diffraction method basically investigates the average crystal structure while local crystal symmetry, defects and disorders in oxides can be better understood by Raman spectroscopy tool [18]. Fig. 3 the figure shows the deconvoluted spectra within the wavelength range 200–800 cm^{-1}; (inset) image represents the spectra for full wavelength range. Theoretical analysis confirms the presence of 13 Raman active modes ($4A_1 + 9E$) in perovskite $BiFeO_3$ structure [19]. This present ceramic (BTO-40) having the same symmetry, so the same set of the Raman active modes should be expected here also. In the inset image there only four characteristic Raman peak near 264, 480, 680 and 1324 cm^{-1}, are clearly observed. But it can be a deconvoluted (using a

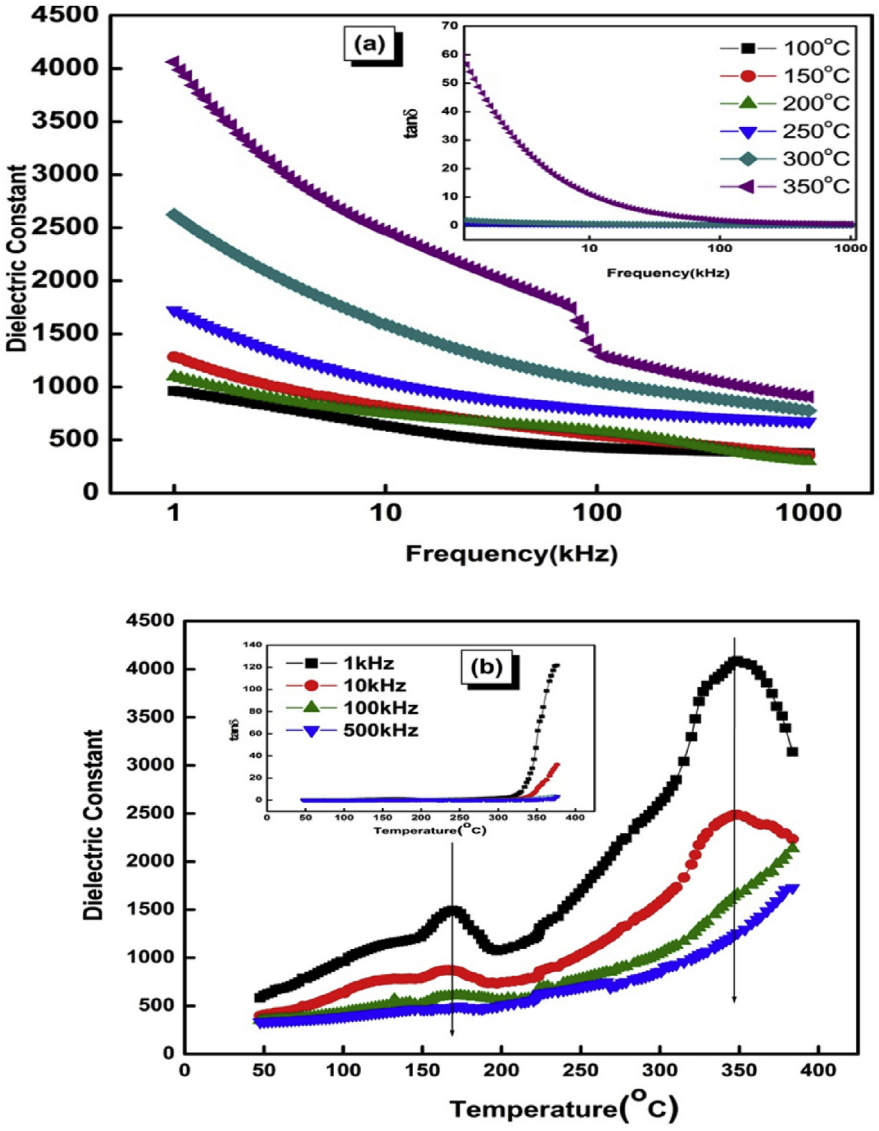

Fig. 4. (a) Frequency dependent permittivity and (inset) loss factor at selected temperatures (b) Temperature dependent permittivity and (inset) loss factor at selected frequencies.

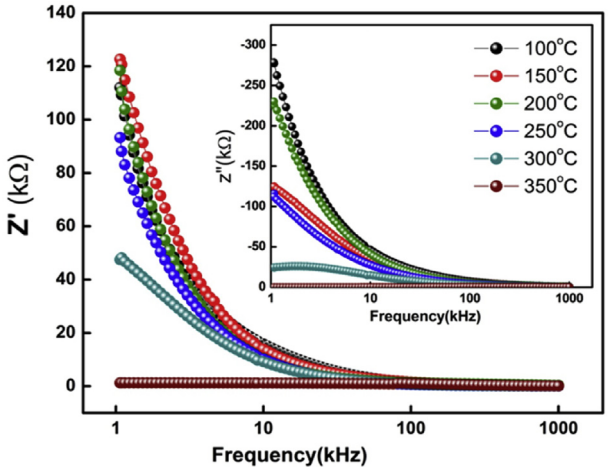

Fig. 5. Frequency dependent real part of impedance and (inset) Frequency dependent imaginary part of the impedance.

Lorentzian function) in six peaks within the wave number range 200–800 cm^{-1} (as shown in the figure). The Raman peaks ~264 cm^{-1} and 480 cm^{-1} corresponds to the E-4 and A_1-4 modes of $BiFeO_3$ structure, respectively. Previously these Raman modes were reported $BiFeO_3$ crystal previously by Fukumura *et al.* [20] The identified Raman band near 680 cm^{-1}, is attributed from the symmetrical stretching vibrations of the oxygen ions of the BO_6 (maybe from GaO_6/TiO_6/FeO_6) octahedra in this ceramics. The similar type of result was similar to the La-doped $BiFeO_3$–$PbTiO_3$ mixed crystal system [21]. The wide Raman peak ~1324 cm^{-1}, corresponds to the arbitrary occupancy of the cations at A-site by Bi/Ba, and at B-site by Fe, Ga and Ti ions, and also the microscopic strains in the ceramics [22].

3.3. Dielectric studies with frequency and temperature

Figure 4 (a) shows the variation of permittivity and loss factor (inset) in the frequency range of 1 kHz to 1 MHz. In the frequency dependent dielectric permittivity, the value of permittivity falls with increment in the frequency, whereas in the lower frequency it attains very high value. The presence of various polarizations may be the reason behind high value at a lower frequency, but as the frequency rises some of them (ionic, dipolar, space-charge) fail to follow the alternating field and their contribution towards permittivity fades or slowly diminishes. Generally, it is well known in the high-frequency region, the electronic polarization is predominant [23]. At the lower frequency range (<10 kHz) a dielectric dispersion is observed while at the higher frequency it attains frequency independent nature or flatness of permittivity commonly termed as the static value of permittivity. The reason behind this is that the electric dipole fails to chase the fast changing alternating field which enhances the friction in between them. Frequency dependent loss factor mainly generated due to crystal lattice imperfection or impurities which lead to polarization to lag behind the alternating field. Dielectric parameters are mainly influenced by the density of prepared material. No relaxation peak is observed in Fig. 4 (a) inset depicting the frequency dependent loss factor. It is observed that at low temperatures, the loss factor is almost constant with very small (<0.1) value, at low frequency (1 kHz) for BFG-BT. But at high temperatures, a sharp increasing trend is seen. This nature of dielectric loss at higher temperature is due to some factors like (i) high temperature sintering leading to the creation of defects, (ii) impurity phase and (iii) charge carriers of the said compound [24].

The Figure 4 (b) represents the variation of permittivity with respect to temperature at selected frequencies. The two peaks are basically seen depicting the existence of both phases (ferroelectric as well as ferrite). The first peak is seen near the Curie temperature of ferroelectric phase while the magnetic transition temperature of ferrite phase is attributed by the second peak. With the rise in temperature leads to the hopping of electrons between Fe^{2+}/Fe^{3+} in ferrite phase generating n-type charge carriers and the hopping of holes between Ba^{3+}/Ba^{2+} in ferroelectric phase generating p-type charge carriers. The local displacement of electrons in the direction of an applied alternating field may influence dielectric polarizations in ferrites. The electron hopping on the octahedral sites between Fe^{+2} and Fe^{+3} ions is responsible for these displacements and conduction. The increase in electric conductivity is caused as electron hopping is thermally activated process [25]. This lead to rise dielectric polarization causing dielectric parameters to reach its maximum magnitude. The highest permittivity is noted to be 4000 at 349 °C for 1 kHz. A further rise in temperature leads to fall in permittivity value because the motion of ions becomes less susceptible in direction of alternating field. The loss factor shoots up at high temperature seen in the inset of Fig. 4 (b). $BiFeO_3$ has an inherent drawback as non-stiochiometric oxygen deficiency leading to space charge polarization in a prepared sample over the entire range of temperature [26]. This effect is prominent because of thermally activated process at high temperature region.

3.4. Impedance analysis

The complex impedance spectroscopy (CIS) is a vital technique which sheds light on the electrical behaviors of the material. The real and imaginary component of impedance distinguishes the true picture of the sample's physical properties. This technique analyses AC response of a system to a sinusoidal perturbation and further impedance is calculated as a function of perturbation frequency. The variation of real component of impedance (Z′) with the frequency at selected temperature is seen in Fig. 5. It is seen with rise in temperature the Z′ rises and falls which depicts typical negative and positive temperature coefficient behavior (NTCR, PTCR) and AC conductivity rises. The real part of impedance monotically decreases with a rise in frequency (>10 kHz) and a constant value is observed (i.e., frequency independent) for all selected

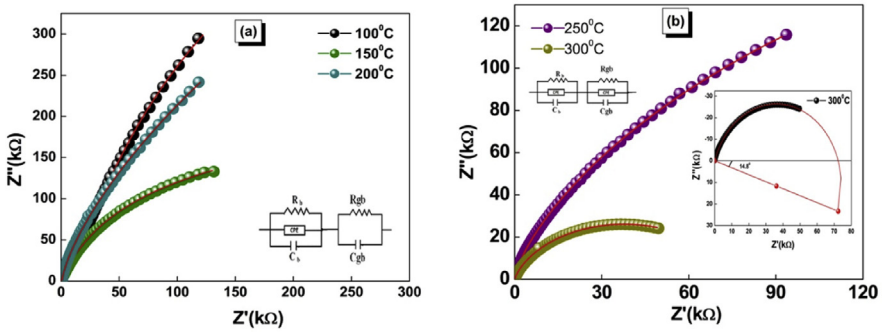

Fig. 6. (a) Variation of Z′ with Z″ at 100 °C, 150 °C, 200 °C and (inset) equivalent circuit model; (b) 250 and 300 °C and (inset) depression angle at 300 °C along with equivalent circuit model of the prepared sample.

Table 2
Comparison of the value of R_g, C_g, R_{gb}, C_{gb} at different temperatures having different model (from Nquist Plot).

Temperature (^{0}C)	Model	$R_g(\Omega)$	C_g (farad)	$R_{gb}(\Omega)$	C_{gb} (farad)
100	(RQC) (RC)	1.097×10^5	2.492×10^{-10}	1.129×10^6	5.426×10^{-10}
150	(RQC) (RC)	4.456×10^5	4.277×10^{-11}	4.448×10^4	2.010×10^{-9}
200	(RQC) (RC)	2.624×10^6	2.602×10^{-10}	8.069×10^2	2.387×10^{-10}
250	(RQC) (RQC)	5.246×10^1	1.000×10^{-23}	6.370×10^5	3.071×10^{-10}
300	(RQC) (RQC)	7.881×10^4	2.894×10^{-10}	4.708×10^1	4.430×10^{-16}

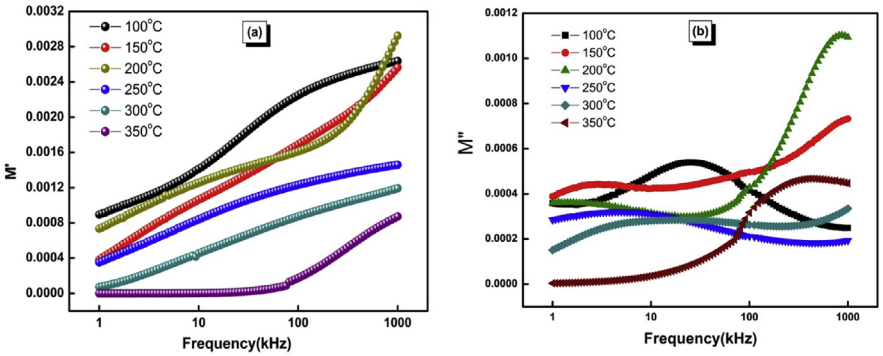

Fig. 7. Frequency dependent (a) real part of modulus and (b) imaginary part of modulus.

temperatures. The trend of merging at higher frequency irrespective of temperature may be due to constant lowering of barrier properties or release of space charge [27]. Fig. 5 inset presents the frequency dependent imaginary component of impedance (Z″). The Z″ variation shows represents the distribution of relaxation time. The electrons/immobile charges are dominant relaxation species at low temperature, whereas at high temperature; this may be the oxygen vacancies or presence of defects. The electrical conductivity may arise due to the hopping of oxygen ion vacancies in localized site [28].

The Nyquist plot suggests the variation of Z′ and Z″ at a few temperatures presented in Fig. 6 (a, b). This plot basically distinguishes the intrinsic (grain), extrinsic (grain boundary) and sample electrode interface contributions to the electrical properties of the material using various circuit elements (resistors, capacitors, inductors, capacitors). The number of semicircular arcs determines the type of electrical process present in the material. The rise of temperature creates depressed semicircle on the real axis with enhancement in temperature due to grain inhomogeneity [29]. It is seen in the inset the equivalent circuit model which is fitted with the experimental data with the help of available computer package known as ZSMIP WIN. It is seen in the Fig. 6 (b) inset

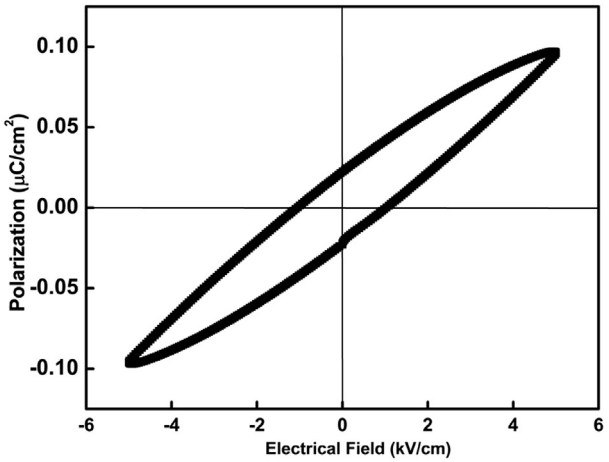

Fig. 8. Room temperature P-E hysteresis loop of the prepared sample.

the depression angle 300 °C is calculated to be 14.8° to the center of the semicircle lying below the real Z axis. By observing the depressed semicircular arc, an existence of a non-Debye type of relaxation mechanism is depicted in the prepared sample. The effect of both grain and grain boundary is observed for all temperatures and the electrical properties illustrated by an electrical network comprising of the parallel combination of (RQC) (RC) for 100, 150, 200 °C and (RQC) (RQC) model for 250, 300 °C where R is resistance, Q is a constant phase element and C is the capacitance. The contribution of grain resistance (R_b), grain capacitance (C_b), grain boundary resistance (R_{gb}) and grain boundary capacitance (C_{gb}) to the total resistance of the compound at some temperatures are compared and estimated in Table 2. The NTCR and PTCR behavior is depicted due to the increasing and decreasing value of R_b and R_{gb} to rise in the temperature [30].

3.5. Complex modulus analysis

Fig. 7 (a, b) shows the variation of real (M′) and imaginary (M″) component of the modulus spectrum with frequency at a few temperatures. At lower frequency, the M′ reaches to zero value, and at the high frequency side, on increasing temperature the M′ curves rise and finally merge illustrating the nonexistence of electrode polarization effect in the sample. The conduction phenomenon may be responsible for this behavior of the M′ and movement of charge carriers of short-range nature which proves that for the mobility of charges there is a deficiency of restoring force due to the effect of a steady electric field [31]. From Fig. 7(b), there is an increase in the temperature peak of M" max (relaxation peak) towards the high frequency region depicting thermally activated nature of relaxation time. The M″ reaches a maximum value at the relaxation frequency. The temperature dependent unsymmetrical M″ peak broadening shows the presence of a non-Debye type of relaxation behavior, which suggest spreading of relaxation with various time constant [32].

3.6. Ferroelectric

Fig. 8 shows the room temperature polarization versus electric field plot for BFG-BT. The ferroelectric hysteresis loop is observed suggesting the nature of the prepared sample to be ferroelectric. The lossy hysteresis

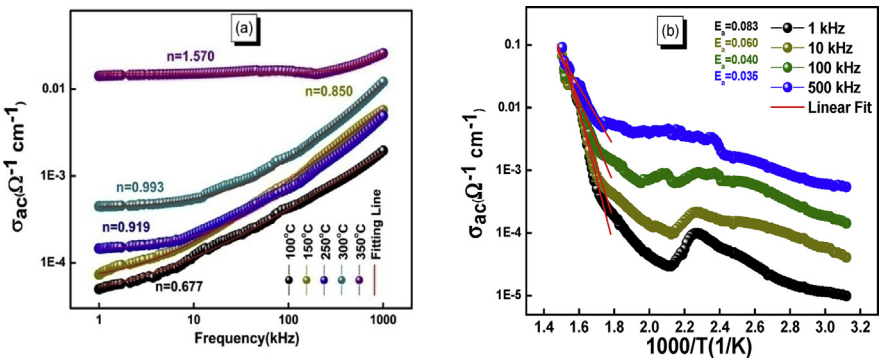

Fig. 9. (a) Frequency dependent AC conductivity with values of power law exponent 'n'. The equation $\alpha_{ac} = A\omega^n$ is used to fit the conductivity plot. (b) Temperature dependence of AC conductivity and E_a represents the value of activation energy at each frequency.

loop is originated due to the oxygen vacancies further to high leakage current in the sample. Generally, in case of the pure BFO at 298 K a well saturated ferroelectric loop is not obtained due to high leakage current created by defects/impurity phases [33]. Furthermore, as BFG-BT is prepared through the high temperature reaction it may have small quantities of oxygen loss which is expressed by the Kroger-Vink [34] notation (Equation 2):

$$O_0^x = V_0^{2+} + \frac{1}{2}O_2 \uparrow + 2e' \tag{2}$$

where, the term O_x represents a loss of lattice oxygen, V_0^{2+} is the existence of oxygen ion vacancy/void and e' is the electron released. The leaky trend of the BFG-BT is due to the presence of oxygen vacancies. The remanent polarization (P_r) is noted to be 0.022 μC/cm^2 at the coercive field of 1.10 kV/cm. Due to high leakage-current nature in BFG-BT, higher electric field cannot be applied.

3.7. Conductivity

The analysis of electrical conductivity helps to investigate the impact of frequency on the electrical properties of the compound as well as the hopping dynamics of ions. The total conductivity (σ_{ac}) of a sample is formulated by dc component and ac component of electric field both dependent on frequency. The ac conductivity can be expressed from the relation given below (Equation 3):

$$\sigma_{ac} = \omega\varepsilon\varepsilon_0 \tan\delta \tag{3}$$

where all the symbols have their usual meanings [35].

The value of conductivity is seen to rise with an increase in frequency and temperature while at lower frequency region it declines. The conductivity dispersion phenomenon is better understood using universal power law by Jonscher (Equation 4) given by

$$\sigma_T = \sigma_{dc} + \sigma_{ac} = \sigma_{dc} + A\omega^n \tag{4}$$

where the low frequency conductivity is determined by σdc, temperature dependent constant is given A, n corresponds to a power law exponent and A is the strength of polarizability [36]. The conduction mechanism can be understood by observing the change of factor 'n' with temperature. If the value of 'n' is constant with respect to temperature rise it is expected to be modeled with quantum mechanical tunnelling model. The small Polaron model is expected if 'n' rises with the temperature rise. If the value of 'n' decreases with the temperature, then correlated barrier hopping is dominant. If 'n' decreases, then increases suggesting overlapping large Polaron tunelling mechanism [37, 38]. From Fig. 9 (a), it is seen that 'n' rises with an enhancement of temperature depicting small Polaron conduction.

Fig. 9 (b) shows the temperature dependent ac conductivity at selected frequencies. The Arrhenius relation (Equation 5) [39]

$$\sigma_{ac} = \sigma_o \exp(-Ea/kB.T) \tag{5}$$

where other symbols have their same meanings determines the activation energy (E_a) values. In this plot, in various temperature regions various slopes for each frequency depicting multiple activation energies [40]. From the Arrhenius plot, in different selected frequency range the conduction mechanism is seen and the corresponding E_a value is 0.083, 0.060, 0.040, 0.035 eV for 1, 10, 100, 500 kHz respectively. As there is an enhancement in temperature and frequency, E_a (activation energy) falls when frequency increases. The movement of oxygen vacancy of longer range nature may contribute towards the conduction mechanism [41]. In the prepared sample, as the temperature rises the conductivity enhances and σ_{ac} also rises with an increase in temperature suggesting thermally activated conduction process. The activation energy may be affected by other factors such as adsorbed and absorbed gasses, crystallite size, lattice defects, variety and quantity of the impurities [42].

4. Conclusion

In summary, the mixed oxide processing and an investigation on composition $0.6Bi(Fe_{0.98}Ga_{0.02})O_3$-$0.4BaTiO_3$ is carried out. The phase analysis of the BFG-BT was performed by XRD confirms the formation of pure phase with few impurity peaks of small intensity. The prepared sample crystallizes in the rhombohedral symmetry. The Scherrer's formula helps to obtain the average crystallite size (42 nm). The morphology of the sintered sample surface reveals the formation of highly dense ceramics. Raman study reveals the local disorder in oxides and various vibrational modes. Dielectric analysis illustrates permittivity and loss factor rises with enhancement of the temperature, and with a rise in frequency the value decreases. The CIS suggests the grain (bulk), grain boundary influences and combined NTCR, PTCR behaviour in the sample. The experimental and fitting parameters (suitable electrical model) of the complex impedance shed light on the capacitive and resistive correlation inside the material. The linear variation of the pattern of conductivity in temperature dependent ac conductivity depicts a thermally activated conduction mechanism. The ac-conductivity study tells that at low temperature the hopping charge carriers are dominant, whereas at temperatures (intermediate and high) the oxygen vacancies are dominant. Thus the study of the above material and its enhancement in electrical properties finds its base for device engineering.

Declarations

Author contribution statement

Sugato Hajra: Performed the experiments; Analyzed and interpreted the data; Wrote the paper.

Manisha Sahu: Conceived and designed the experiments; Analyzed

and interpreted the data.

Varsa Purohit: Performed the experiments.

R. N. P. Choudhary: Contributed reagents, materials, analysis tools or data.

Funding statement

This research did not receive any specific grant from funding agencies in the public, commercial, or not-for-profit sectors.

Competing interest statement

The authors declare no conflict of interest.

Additional information

No additional information is available for this paper.

Acknowledgements

The authors like to mention the kind help of Professor P.K Parida, CET Bhubaneswar and Mr. Manojit De, GGCU Bilaspur, Dr. Ajeet Kumar, DRDO, Hyderabad for some experiments in their laboratory.

References

[1] J. Rödel, K.G. Webber, Robert Dittmer, Wook Jo, M. Kimura, D. Damjanovic, J. Eur. Ceram. Soc. 35 (2015) 1659–1681.
[2] J. Rödel, Wook Jo Klaus, T.P. Seifert, Eva-maria Anton, T. Granzow, D. Damjanovic, J. Am. Ceram. Soc. 92 (2009) 1153–1177.
[3] T. Ibn-Mohammed, S.C.L. Koh, I.M. Reaney, C.A. Acquaye, D. Wang, S. Taylore, A. Genovesef, Energy Environ. Sci. 9 (2016) 3495–3520.
[4] S.O. Leontsev, R.E. Eitel, Sci. Technol. Adv. Mater. 11 (2010), 044302.
[5] M.H. Lee, Da Jeong Kim, J Su Park, S.W. Kim, Tae Kwon Song, M-Ho Kim, W.-J. Kim, D. Do, Il-Kyoung Jeong, Adv. Mater. 27 (2015) 6976–6982.
[6] D.S. Keeble, E.R. Barney, D.A. Keen, M.G. Tucker, Jens Kreisel, P.A. Thomas, J. Am. Ceram. Soc. 23 (2013) 185–190.
[7] C. Blaauw, F. van der Woude, J. Phys. C Solid State Phys. 6 (1973) 1422.
[8] G. Catalan, J.F. Scott, Adv. Mater. 21 (2009) 2463–2485.
[9] T. Rojac, A. Bencan, B. Malic, G. Tutuncu, J.L. Jones, J.E. Daniels, D. Damjanovic, J. Am. Ceram. Soc. 97 (2014) 1993–2011.
[10] L. Wang, C.-H. Yang, J. Wen, Electron. Mater. Lett. 11 (2015) 505–543.
[11] S.O. Leontsev, R.E. Eitel, J. Am. Ceram. Soc. 92 (2009) 2957–2961.
[12] M.M. Kumar, A. Srinivas, S.V. Suryanarayana, J. Appl. Phys. 87 (2000) 855–862.
[13] J.R. Cheng, N. Li, L. Eric Cross, J. Appl. Phys. 94 (2003) 5153–5157.
[14] Min-Jia Wang, H. Yang, Qi-L. Zhang, Zhi-S. Lin, Zi-Shan Zhang, Dan Yu, Liang Hu, Mater. Res. Bull. 60 (2014) 485–491.
[15] Matjaz Valant, A.-K. Axelsson, Neil Alford, Chem. Mater. 19 (2007) 5431–5436.
[16] C. Behera, Piyush R. Das, R.N.P. Choudhary, J. Electron. Mater. 43 (2014) 3539–3549.
[17] D.C.L. Vasconcelos, V.C. Costa, E.H.M. Nunes, A.C.S. Sabioni, M. Gasparon, W.L. Vasconcelos, Mater. Sci. Appl. 2 (2011) 1375–1382.
[18] R. Medwal, S. Gupta, S.P. Pavunny, R.K. Katiyar, S. Annapoorni, R.S. Katiyar, Mater. Lett. 160 (2015) 183.
[19] D. Kothari, V. Raghavendra Reddy, V.G. Sathe, A. Gupta, A. Banerjee, A.M. Awasthi, J. Magn. Magn. Mater. 320 (2008) 548–552.
[20] H. Fukumura, H. Harima, K. Kisoda, M. Tamada, Y. Noguchi, M. Miyayama, J. Magn. Magn. Mater. 310 (2007) 367–369.
[21] K.K. Mishra, V. Sivasubramanian, R.M. Sarguna, T.R. Ravindran, A.K. Arora, J. Solid State Chem. 184 (2011) 2381–2386.
[22] A. Ianculescu, L. Mitoseriu, H. Chiriac, M.M. Carnasciali, A. Braileanu, R. Trusca, J. Optoelectron. Adv. Mater. 10 (2008) 1805–1809.
[23] S. Hajra, S. Sahoo, R. Das, R.N.P. Choudhary, J. Alloy. Comp. 750 (2018) 507–514.
[24] S. Sen, R.N.P. Choudhary, Mater. Chem. Phys. 87 (2004) 256–263.
[25] C.G. Koops, Phys. Rev. 83 (1951) 121–124.
[26] T. Ito, T. Ushiyama, M. Aoki, Y. Tomioka, Y. Hakuta, H. Takashima, R. Wang, Inorg. Chem. 52 (2013) 12806–12810.
[27] C.K. Suman, K. Prasad, R.N.P. Choudhary, J. Mater. Sci. 41 (2006) 369.
[28] A.K. Jonscher, Nature 267 (1977) 673–679.
[29] Z. Dai, Y. Akishige, J. Phys. D Appl. Phys. 43 (2010) 445403.
[30] M. Chandrasekhara, D.K. Khatua, R. Pattanayak, P. Kumar, J. Phys. Chem. Solids 111 (2017) 160–166.
[31] V. Provenzano, L.P. Boesch, V. Volterra, C.T. Moynihan, P.B. Macedo, J. Am. Ceram. Soc. 55 (1972) 492–496.
[32] M. De, Sugato Hajra, R. Tiwari, S. Sahoo, R.N.P. Choudhary, H.S. Tiwari, Ceram. Int. 44 (2018) 11792–11797.
[33] Qi Zhang, D. Sando, V. Nagarajan, J. Mater. Chem. C 4 (2016) 4092–4124.
[34] S. Nath, S.K. Barick, S. Hajra, R.N.P. Choudhary, J. Mater. Sci. Mater. Electron. 29 (2018) 12251–12257.
[35] V. Purohit, R. Padhee, R.N.P. Choudhary, Ceram. Int. 44 (2018) 3993–3999.
[36] S.R. Elliot, Phil. Mag. 36 (1977) 1291–1304.
[37] T.M. Meaz, S.M. Attia, A.M. Abo El Ata, J. Magn. Magn. Mater. 257 (2003) 296–305.
[38] A. Ghosh, Phys. Rev. B 42 (1990) 1388–1392.
[39] K. Parida, S.K. Dehury, R.N.P. Choudhary, Phys. Lett. 380 (2016) 4083–4091.
[40] Sugato Hajra, A. Tripathy, B.K. Panigrahi, R.N.P. Choudhary, Mater. Res. Express 6 (2019), 076304.
[41] H. Jain, C.H. Hsieh, J. Solids Non Cryst 1408 (1994) 172–174.
[42] N.M.A. Hadia, M.F. Hasaneen, M.A. Hassan, S.H. Mohamed, J. Mater. Sci. Mater. Electron. 29 (2017) 4155–4162.